Research Square

Preprints are preliminary reports that have not undergone peer review.
They should not be considered conclusive, used to inform clinical practice,
or referenced by the media as validated information.

Quantifying Spatial Cross-Validation Inflation in Satellite-Ground Air Quality Coupling: Mesoscale NDVI/LST Regimes and Land Use Regression Across an Urban Megacity

Saptarshi Sadhu

saptarshi1.sadhu@stu.adamasuniversity.ac.in

Adamas University https://orcid.org/0009-0009-7505-1973

Research Article

Keywords: urban vegetation gradients, PM2.5 exposure, particulate matter, Kolkata airshed, temporal holdout validation, Landsat-8/9 OLI/TIRS, spatial cross-validation

Posted Date: November 20th, 2026

DOI: https://doi.org/10.21203/rs.3.rs-11793536/v1

License: This work is licensed under a Creative Commons Attribution 4.0 International License.
Read Full License

Additional Declarations: The authors declare no competing interests.

Quantifying Spatial Cross-Validation Inflation in Satellite-Ground Air Quality Coupling: Mesoscale NDVI/LST Regimes and Land Use Regression Across an Urban Megacity

Saptarshi Sadhu[1*]

[1]School of Engineering and Technology, Adamas University, Kolkata 700126, West Bengal, India

ORCID: https://orcid.org/0009-0009-7505-1973

[*]Correspondence: saptarshi1.sadhu@stu.adamasuniversity.ac.in

Abstract

Coupling satellite remote sensing with ground telemetry enhances urban exposure modeling, yet conventional protocols frequently suffer from cross-validation inflation. We evaluate Landsat-8/9 Operational Land Imager (OLI, 30 m) and Thermal Infrared Sensor (TIRS, 100 m resampled to 30 m) imagery coupled with a 13-station regulatory network across Kolkata during 2024–2025 (16.1 million continuous records; 731 station-days, $N = 1,108$). Multi-spectral surface indicators—Normalized Difference Vegetation Index (NDVI), Normalized Difference Built-up Index (NDBI), McFeeters open-water Normalized Difference Water Index (NDWI), and Land Surface Temperature (LST)—were quantified across 3 km buffers. Industrial corridors exhibited intense thermal stress (LST : 33.27–36.73°C) and low greenness (NDVI : 0.1007–0.1496), coinciding with peak particulate concentrations ($PM_{2.5}$: 47.97–69.16 μg m^{-3}). Conversely, vegetative parkland buffers maintained higher greenness (NDVI : 0.1877–0.2091), 3.0–4.5°C lower skin temperatures, and a 71.8% observational reduction in row-weighted $PM_{2.5}$ relative to industrial corridors. Benchmarking four Land Use Regression paradigms reveals critical divergence: contemporaneous random cross-validation yields an inflated $R^2 = 0.6790$ (root mean squared error, RMSE = 22.05 μg m^{-3}) relative to Temporal GroupKFold ($R^2 = 0.4564$; isolating a $\Delta R^2 = 0.2226$ date-leakage penalty) and Spatial Station Group Holdout ($R^2 = 0.4059$; a $\Delta R^2 = 0.0505$ spatial extrapolation penalty), while forward transfer (2024 $\rightarrow$ 2025) yields $R^2 = 0.3636$ under Ordinary Least Squares (OLS) and $R^2 = 0.3177$ under Random Forest. Thermal emissions (49.80%) and McFeeters NDWI (19.91%) govern predictor importance, demonstrating that blocked spatiotemporal validation protocols are essential to prevent over-optimistic performance claims.

Keywords: urban vegetation gradients; PM2.5 exposure; particulate matter; Kolkata airshed; temporal holdout validation; Landsat-8/9 OLI/TIRS

Introduction

Urban land-cover transformation profoundly modifies surface energy partitioning, microclimatic thermal regimes, and aerodynamic pollutant dispersion in developing metropolitan conurbations (Oke, 1982; Yin et al., 2023; Wang et al., 2018). Replacement of natural vegetation and open waterbodies with dense impervious infrastructure elevates sensible heat flux and suppresses evaporative cooling, exacerbating surface Urban Heat Islands (UHIs) and generating localized microclimatic thermal stress (Moonen et al., 2012; Xie et al., 2016). Simultaneously, complex interactions between surface roughness, thermal inversions, and localized emission sources create severe particulate matter ($PM_{2.5}$) non-attainment hotspots across South Asian megacities, posing chronic risks to respiratory and cardiovascular health (Lelieveld et al., 2015; Cohen et al., 2017; World Health Organization, 2021). Understanding how mesoscale blue–green infrastructure modulates ambient air quality is therefore a pressing priority for urban environmental science and sustainable spatial planning (Dasgupta et al., 2013; Sarkar et al., 2021; Chakroborty et al., 2025).

Coupling multi-spectral satellite remote sensing with ground-based continuous ambient air quality monitoring provides a powerful methodology to characterize these environmental gradients (Hoek et al., 2008; Deguen and Zmirou-Navier, 2010). Satellite sensors capture high-resolution spatial proxies of land surface biophysics, including spectral greenness via the Normalized Difference Vegetation Index (NDVI), built-up imperviousness via the Normalized Difference Built-up Index (NDBI), open-water coverage via the Normalized Difference Water Index (NDWI), and thermal radiation via Land Surface Temperature (LST) (Zha et al., 2003; McFeeters, 1996; Sobrino et al., 2004; Wang et al., 2018). Integrating these satellite-derived surface metrics into Land Use Regression (LUR) and machine learning architectures enables spatial exposure estimation across heterogeneous urban landscapes.

However, standard spatial regression models and machine learning implementations frequently suffer from severe, unacknowledged cross-validation inflation (Anselin, 1995; Hengl et al., 2017; Meyer et al., 2018; Ploton et al., 2020). When satellite-ground observations from fixed monitoring networks are evaluated using conventional random k-fold cross-validation, records collected on identical calendar dates are randomly allocated across training and test splits. Because synoptic weather regimes (boundary-layer mixing height, regional humidity, wind velocity, and air mass stagnation) are shared conurbation-wide on any given satellite overpass day, random partitioning permits pervasive temporal information leakage between folds. Consequently, random cross-validation tests the model's capacity to interpolate under known synoptic conditions rather than evaluating true spatial generalizability to unmonitored locations. To date, the exact empirical magnitude of this cross-validation inflation has not been systemat-

ically quantified in tropical riverine megacities where sharp land-use boundaries and complex thermal gradients coexist.

Literature Review: Blue–Green Infrastructure, Thermal Regimes, and Air Quality

Prior investigations have characterized urban land cover, surface thermal regimes, and air quality across diverse metropolitan settings (Kikon et al., 2016; Mathew et al., 2017; Kumar et al., 2020; Sultana and Satyanarayana, 2020; Halder et al., 2021; Jang et al., 2024; Islam et al., 2024; O'Regan et al., 2024; Hong et al., 2025; Su et al., 2026). Across Indian cities, multi-temporal satellite investigations have demonstrated that replacing vegetative cover and wetlands with dense impervious surfaces systematically depresses latent heat flux while intensifying surface UHIs, including across Noida (Kikon et al., 2016), Jaipur (Mathew et al., 2017), and Chandigarh using Landsat-derived spectral indices (Sultana and Satyanarayana, 2020). Within the Kolkata–Howrah megacity specifically, foundational investigations have characterized urban thermal dynamics: Halder et al. (2021) utilized multi-temporal Landsat-8 OLI/TIRS observations to document built-up expansion and the proliferation of $> 35\,^{\circ}\mathrm{C}$ thermal hotspots across Kolkata and adjacent Howrah, while Islam et al. (2024) investigated the non-linear cooling efficacy and threshold dynamics of urban blue–green infrastructure using Landsat metrics and machine learning. Concurrently, Kumar et al. (2020) analyzed criteria particulate matter ($PM_{2.5}$) dynamics across major Indian cities including Kolkata, highlighting the influence of boundary-layer meteorology and anthropogenic emission shifts, while subsequent local ground studies characterized $PM_{2.5}$ chemical composition and oxidative potential (Bera et al., 2020; Sarkar et al., 2021; Ghosh et al., 2023, 2024; Chakroborty et al., 2025).

In recent international research (2024–2026), advanced machine learning ensembles and interpretable artificial intelligence have been deployed to isolate complex non-linear interactions among urban infrastructure, microclimate, and air pollution. In Seoul, South Korea, Jang et al. (2024) deployed high-density urban sensor networks and spatial regression to evaluate street-level thermal comfort (UTCI) and microclimate cooling, while Hong et al. (2025) analyzed 568 IoT sensors with Random Forest to resolve non-linear interactions between three-dimensional urban morphology and synoptic weather forcing. In Cork, Ireland, O'Regan et al. (2024) demonstrated enhanced urban NO_2 exposure mapping by fusing citizen-science passive sampling with dispersion models. Most recently, Su et al. (2026) demonstrated that multidimensional urban morphological parameters exhibit distinct non-linear threshold effects on six criteria air pollutants across arid urban regimes, complementing international street-canyon aerodynamic reviews (Janhäll, 2015; Selmi et al., 2016; Abhijith et al., 2017; Han et al., 2018; Barwise and Kumar, 2020; Tomson et al., 2021; Shen et al., 2024; Yao et al., 2025).

Despite these advances, existing satellite-ground exposure studies predominantly rely on random cross-validation, obscuring the degree to which shared-date synoptic autocorrelation

inflates reported predictive skill. Table 1 synthesizes representative literature and delineates the specific analytical gap addressed by this investigation.

Table 1. Synthesis of representative literature on urban thermal regimes, blue–green infrastructure (BGI), and air quality modeling.

Study	Study Area	Sensors & Methods	Primary Focus & Analytical Gap Addressed Here
Kikon et al. (2016); Mathew et al. (2017)	Noida & Jaipur, India	Landsat, MODIS, regression	Quantified NDVI, NDBI, and emissivity controls on UHI; did not couple ground criteria air pollutants or LUR models.
Sultana and Satyanarayana (2020)	Chandigarh, India	Landsat (2000–2018; EBBI, DBI, DBSI, NDVI)	Assessed long-term LULC and seasonal UHI intensity; did not integrate ground air quality telemetry.
Kumar et al. (2020)	Kolkata & 4 Indian cities	Ground CAAQMS $PM_{2.5}$ & meteorology	Quantified $PM_{2.5}$ responses to emission shifts across Indian cities; did not couple satellite LST, NDVI, or NDBI buffers.
Halder et al. (2021)	Kolkata & adjacent Howrah, India	Landsat-8 OLI/TIRS (NDVI, NDBI, NDWI, LST)	Mapped UHI hotspots (> 35 °C) and vegetative loss in Kolkata–Howrah; did not integrate ground air quality stations or LUR.
Jang et al. (2024)	Seoul, South Korea	Urban IoT sensor network, UTCI, spatial regression	Evaluated street-level GI cooling and thermal comfort; did not model particulate or gaseous air pollutants.
Islam et al. (2024)	Kolkata, India	Landsat BGI metrics, Random Forest & XAI	Quantified non-linear BGI surface cooling in Kolkata; did not integrate CAAQMS air pollution telemetry or audit LUR CV leakage.
O'Regan et al. (2024)	Cork, Ireland	Citizen-science NO_2 & dispersion data fusion	Enhanced urban NO_2 mapping via data fusion; did not evaluate satellite thermal/vegetative thresholds on $PM_{2.5}$.
Hong et al. (2025)	Seoul, South Korea	568 IoT sensors, Random Forest & SHAP	Isolated non-linear urban–meteorological interactions on street-level UHI; did not model criteria air pollutants or forward temporal transfer.
Su et al. (2026)	Ürümqi–Changji–Shihezi, China	ML regression, SHAP, 6 criteria pollutants	Identified non-linear urban morphology thresholds on $PM_{2.5}$ and O_3 in a dry-hot region; did not audit shared-date synoptic CV leakage.
Present Study (2024–2025)	**Kolkata–Howrah (13 CAAQMS)**	**Landsat-8/9 OLI/TIRS 3 km buffers + CAAQMS $PM_{2.5}$**	**Couples multi-spectral indices (NDVI, NDBI, NDWI, LST) with ground telemetry; benchmarks spatial, temporal, and forward cross-validation leakage.**

Research Objectives and Scope

To resolve these critical geospatial and environmental modeling gaps, this investigation establishes three primary scientific objectives:

1. Characterize the spatiotemporal distributions of multi-spectral surface indices (NDVI, NDBI, NDWI) and radiometric Land Surface Temperature (LST) across 3 km mesoscale buffers encompassing 13 statutory CAAQMS monitoring stations during 2024–2025;

2. Benchmark Land Use Regression (LUR) generalization performance across four rigorous validation paradigms: contemporaneous random 5-fold cross-validation, spatial station-grouped holdout, temporal date-grouped holdout, and forward chronological transfer (2024 → 2025), quantifying the exact magnitude of spatial cross-validation inflation;

3. Quantify empirical particulate concentration gradients across satellite greenness brackets, establishing the non-linear relationship between mesoscale canopy greenness, open-water coverage, and ground $PM_{2.5}$ dilution in a tropical megacity airshed.

Materials and Methods

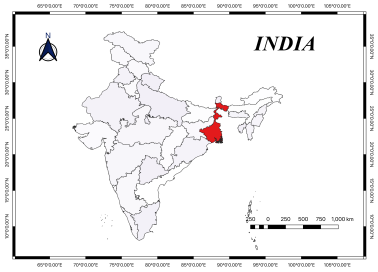
Study Area and 13 CAAQMS Monitoring Network

The Kolkata Metropolitan Area (KMA) is situated in eastern India along the lower deltaic reaches of the Ganges (Hooghly) River basin (22.4°N–22.8°N, 88.2°E–88.5°E; elevation 6–11 m above mean sea level). The regional climate is classified as tropical wet-and-dry (Köppen Aw), characterized by hot pre-monsoon summers (March–May), southwest summer monsoon precipitation (June–September), post-monsoon transitions (October–November), and cool, stable winters (December–February) (Dasgupta et al., 2013). The airshed is physically bisected by the tidal Hooghly River: the western bank (Howrah district) comprises dense metallurgy, foundries, and freight transit hubs, while the eastern bank (Kolkata district) encompasses high-density commercial, institutional, residential, and urban parkland sectors (Chakroborty et al., 2025).

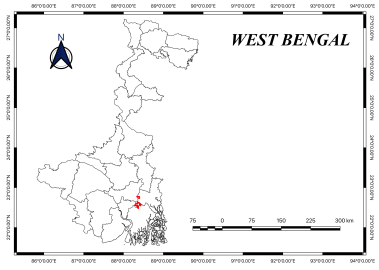
Continuous ground-level atmospheric telemetry was curated across all 13 statutory CAAQMS monitoring stations operated by the Central Pollution Control Board (CPCB) and West Bengal Pollution Control Board (WBPCB). Fig. 1 illustrates the regional airshed and monitoring network configuration. Table 2 summarizes the geographic coordinates, operational elevation, Local Climate Zone (LCZ) classifications, and dominant built-environment drivers across all 13 stations. Ground telemetry encompasses continuous measurements of fine particulate matter ($PM_{2.5}$), coarse particulate matter (PM_{10}), nitrogen oxides (NO, NO_2, NO_x), sulfur dioxide (SO_2), and surface meteorology. Fine particulate mass ($PM_{2.5}$) is quantified via Beta Attenuation Monitoring (BAM-1020, Met One Instruments) at a volumetric flow rate of 16.67 L min^{-1} with sample stream heating to prevent hygroscopic moisture artifacts. Bi-weekly automated zero/span calibration and multi-sigma quality screening protocols were enforced to eliminate power-interruption artifacts (Vohra et al., 2025).

Table 2. CAAQMS Monitoring Network across 13 Stations in Kolkata and Howrah: Verified Geodetic Coordinates, Operational Elevation, Zone Classifications, and Dominant Built Environment Drivers.

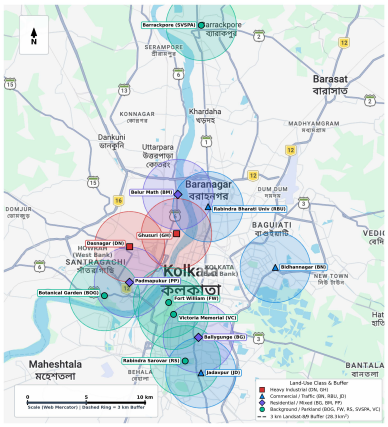
Station Name	Code	Latitude	Longitude	Elevation	Zone Classification	Dominant Built Environment Drivers
Ballygunge	BG	22.5264°N	88.3692°E	8 m	High-Density Residential	Compact mid-rise residential fabric, dense vehicular grid, paved corridors
Barrackpore	SVSPA	22.7661°N	88.3644°E	11 m	Industrial / Suburban Mixed	Paper mills, textile manufacturing, suburban open canopy, perimeter forest
Belur Math	BM	22.6362°N	88.3521°E	9 m	Religious / Riverine Mixed	Riparian riverbank frontage, adjacent metal fabrication and foundry belt
Bidhannagar	BN	22.5802°N	88.4331°E	6 m	Commercial IT Corridor	Modern planned commercial sector, glass-facade IT parks, wide asphalt avenues
Botanical Garden	BOG	22.5473°N	88.2941°E	7 m	Protected Green Background	Historic botanical garden, extensive multi-layered tree canopy, river frontage
Dasnagar	DN	22.5921°N	88.3053°E	8 m	Heavy Industrial Corridor	Iron and steel foundries, casting workshops, unpaved roads, high thermal emission
Fort William	FW	22.5532°N	88.3444°E	9 m	Urban Parkland / Military	Extensive manicured grassland (Maidan), canopy trees, central traffic arterial bypass
Ghusuri	GH	22.5824°N	88.3163°E	7 m	Heavy Industrial Corridor	Dense metal recycling, rerolling mills, glass furnaces, heavy freight traffic
Jadavpur	JD	22.4991°N	88.3713°E	7 m	Mixed Urban / Educational	University campus green patches embedded in dense, low-rise commercial street canyons
Padmapukur	PP	22.5651°N	88.3072°E	6 m	Industrial / Residential Mixed	Municipal water treatment works, large open water reservoirs, local foundry proximity
Rabindra Bharati Univ	RBU	22.5932°N	88.3724°E	8 m	Heavy Traffic Hotspot	Major arterial intersection (BT Road), continuous heavy bus/truck transit, asphalt
Rabindra Sarovar	RS	22.5083°N	88.3582°E	7 m	Urban Park Background	Urban national lake system (73 hectares), perimeter jogging tree canopy, residential
Victoria Memorial	VC	22.5441°N	88.3432°E	8 m	Urban Heritage Background	Formal memorial gardens, protected parkland buffer, central urban microclimate oasis



(a) National Geographic Setting (India)



(b) State Airshed Context (West Bengal)



(c) CAAQMS Stations and Buffers

Fig. 1 Geographic setting and monitoring network configuration of the Kolkata–Howrah conurbation: (a) Regional location within the lower Indo-Gangetic Plain; (b) Airshed setting across West Bengal; (c) Spatial distribution of 13 statutory CAAQMS monitoring stations across Kolkata and Howrah with uniform 3 km radial buffers

Satellite Remote Sensing Data and Zonal Buffer Extraction

High-resolution optical surface reflectance and thermal emissions were acquired from USGS Landsat-8 and Landsat-9 Collection-2 Level-2 Operational Land Imager (OLI) and Thermal Infrared Sensor (TIRS) overpasses over Path 138 / Row 44 across calendar years 2024 and 2025. Optical reflectance bands (Band 3 Green, Band 4 Red, Band 5 Near-Infrared, and Band 6 Shortwave-Infrared) provide 30 m ground sampling distance. Thermal infrared radiance (TIRS Band 10) was resampled from native 100 m resolution to 30 m grid alignment with standard radiometric calibration and atmospheric correction. Pixel-level pixel quality assessment (QA) bands were utilized to mask clouds, cloud shadows, and cirrus artifacts, supplemented by an empirical surface temperature quality filter ($\mathrm{LST}_C > 10.0^\circ\mathrm{C}$).

To characterize the surrounding built and vegetative environment, zonal extractions were computed across uniform 3 km radial buffers centered on each CAAQMS monitoring station. The 3 km mesoscale radius captures neighborhood-scale land use, canopy density, impervious coverage, and riparian influences governing local ventilation corridors. Across the 2024–2025 observation window, this protocol yielded $N = 1,108$ aligned scene-station extractions across 731 unique station-days (333 station-days with 479 extractions in 2024; 398 station-days with 629 extractions in 2025). Ground $\mathrm{PM}_{2.5}$ concentrations were matched to satellite overpasses as calendar-day arithmetic means adhering to $\geq 75\%$ temporal completeness criteria.

Spectral Built Environment Indices and Thermal Formulation

Photosynthetically active vegetative greenness was quantified via the Normalized Difference Vegetation Index (NDVI) using red (ρ_{Red}, Band 4) and near-infrared (ρ_{NIR}, Band 5) surface

reflectance:

$$\mathrm{NDVI} = \frac{\rho_{\mathrm{NIR}} - \rho_{\mathrm{Red}}}{\rho_{\mathrm{NIR}} + \rho_{\mathrm{Red}}} = \frac{\mathrm{Band\ 5} - \mathrm{Band\ 4}}{\mathrm{Band\ 5} + \mathrm{Band\ 4}} \tag{1}$$

Impervious building and pavement footprints were quantified via the Normalized Difference Built-up Index (NDBI) using shortwave-infrared reflectance (ρ_{SWIR1}, Band 6, 1.57–1.65 μm) relative to near-infrared (Zha et al., 2003):

$$\mathrm{NDBI} = \frac{\rho_{\mathrm{SWIR1}} - \rho_{\mathrm{NIR}}}{\rho_{\mathrm{SWIR1}} + \rho_{\mathrm{NIR}}} = \frac{\mathrm{Band\ 6} - \mathrm{Band\ 5}}{\mathrm{Band\ 6} + \mathrm{Band\ 5}} \tag{2}$$

Surface waterbodies and riverine channels were delineated via the Normalized Difference Water Index formulated by McFeeters (1996):

$$\mathrm{NDWI} = \frac{\rho_{\mathrm{Green}} - \rho_{\mathrm{NIR}}}{\rho_{\mathrm{Green}} + \rho_{\mathrm{NIR}}} = \frac{\mathrm{Band\ 3} - \mathrm{Band\ 5}}{\mathrm{Band\ 3} + \mathrm{Band\ 5}} \tag{3}$$

McFeeters NDWI exploits the elevated reflectance of green light and near-complete absorption of near-infrared radiation by liquid water to maximize the contrast of open surface water features (such as the Hooghly River, wetlands, and municipal reservoirs). It is fundamentally distinct from shortwave-infrared foliar water indices ($\frac{\rho_{\mathrm{NIR}} - \rho_{\mathrm{SWIR}}}{\rho_{\mathrm{NIR}} + \rho_{\mathrm{SWIR}}}$), which track foliar canopy water thickness. In this study, buffer-averaged McFeeters NDWI quantifies open surface water coverage within the 3 km mesoscale buffer.

Radiometric Land Surface Temperature (LST, °C) was retrieved from Landsat-8/9 Thermal Infrared Sensor (TIRS Band 10) observations, resampled from native 100 m sensor resolution to 30 m grid alignment with standard scale and offset calibrations, and screened for clear-sky quality flags ($\mathrm{LST}_C > 10.0$°C). Across the 13 monitoring stations, mesoscale buffer-averaged LST characterizes the surrounding surface thermodynamic regime, integrating impervious thermal storage, latent heat depression, and anthropogenic heat rejection.

Land Use Regression Framework and Algorithmic Implementations

Land Use Regression (LUR) models map the satellite buffer feature vector $\mathbf{x}_i = [\mathrm{NDVI}_i, \mathrm{NDBI}_i, \mathrm{NDWI}_i, \mathrm{LST}_i]^\top$ onto ground $\mathrm{PM}_{2.5}$ concentration (y_i, μg m^{-3}) at station-date i:

$$y_i = f(\mathbf{x}_i) + \varepsilon_i \tag{4}$$

where ε_i is stochastic residual error. Ordinary Least Squares (OLS) multiple linear regression provides the parametric baseline:

$$y_i = \beta_0 + \sum_{k=1}^{K} \beta_k x_{ik} + \varepsilon_i, \quad \hat{\boldsymbol{\beta}} = (\mathbf{X}^\top \mathbf{X})^{-1} \mathbf{X}^\top \mathbf{y} \tag{5}$$

Support Vector Regression (SVR) with a Radial Basis Function (RBF) kernel fits a non-linear hyperplane under the ϵ-insensitive loss function ($C = 1.0, \epsilon = 0.1, \gamma = \text{scale}$). Continuous satellite predictors were standardized (zero mean, unit variance via z-score scaling) strictly within each training fold prior to kernel evaluation, with test folds transformed using training fold parameters to prevent cross-validation scale leakage:

$$f(\mathbf{x}) = \sum_{i=1}^{N} (\alpha_i - \alpha_i^*) \exp\left(-\gamma \|\mathbf{x}_i - \mathbf{x}\|^2\right) + b \tag{6}$$

The Random Forest Regressor (RF) averages $B = 100$ de-correlated decision trees $\{T_1, \ldots, T_B\}$ (random state = 42) (Hengl et al., 2017):

$$\hat{f}_{\text{RF}}(\mathbf{x}) = \frac{1}{B} \sum_{b=1}^{B} T_b(\mathbf{x}) \tag{7}$$

Predictor importance within the Random Forest ensemble was quantified via mean decrease in impurity (MDI / variance-reduction importance for regression, measuring the reduction in residual sum of squares across tree splits), normalizing relative contributions across the four multi-spectral predictors to sum to 100%.

Validation Frameworks and Cross-Validation Leakage Auditing

To address the pervasive challenge of spatial autocorrelation and synoptic date leakage in spatiotemporal environmental models (Anselin, 1995; Hengl et al., 2017; Meyer et al., 2018; Ploton et al., 2020), Land Use Regression performance was evaluated across four distinct validation frameworks encompassing 1,108 aligned station-date observations (479 in 2024 and 629 in 2025).

In the first paradigm, contemporaneous random 5-fold cross-validation randomly partitions the pooled observations into five subsets irrespective of monitoring location or overpass date. Because monitoring stations across the conurbation share identical overpass dates within any fold, this conventional baseline evaluates interpolation under shared regional synoptic weather conditions.

In the second paradigm, the spatial station-grouped evaluation partitions observations strictly by monitoring-station identity (`groups = df['station']`) across 5 folds using `GroupKFold`. This framework evaluates true spatial generalization when complete monitoring stations are held out from model training, testing performance at unmonitored geographic coordinates.

In the third paradigm, Temporal GroupKFold groups observations strictly by satellite overpass date, holding out all stations across unseen calendar dates to assess conurbation-wide generalization on unobserved overpass days without forward temporal ordering (Meyer et al., 2018).

In the fourth paradigm, forward temporal transfer simulates real-world operational forecast-

ing by enforcing strict chronological partitioning: models are trained exclusively on all calendar year 2024 observations ($N = 479$) and evaluated on all subsequent calendar year 2025 observations ($N = 629$).

Model performance across all frameworks was evaluated using the Coefficient of Determination (R^2), Root Mean Squared Error (RMSE, μg m^{-3}), and Mean Absolute Error (MAE, μg m^{-3}):

$$R^2 = 1 - \frac{\sum_{i=1}^{N}(y_i - \hat{y}_i)^2}{\sum_{i=1}^{N}(y_i - \bar{y})^2} \tag{8}$$

$$\text{RMSE} = \left[\frac{1}{N}\sum_{i=1}^{N}(y_i - \hat{y}_i)^2\right]^{1/2} \tag{9}$$

$$\text{MAE} = \frac{1}{N}\sum_{i=1}^{N}|y_i - \hat{y}_i| \tag{10}$$

where y_i represents the observed ground concentration, $\hat{y}_i$ denotes the model prediction, and $\bar{y}$ is the empirical sample mean of the evaluation split.

Computational Framework and AI Disclosure

All satellite raster processing, buffer extraction, statistical modeling, and cross-validation pipelines were implemented in Python 3.13 using rasterio, geopandas, NumPy, SciPy, and Scikit-Learn. Generative AI tools (Anthropic Claude and Google Gemini) assisted substantially in computational script development, mathematical formalization, structuration of theoretical linkages, and manuscript drafting and language editing. The author conceived the research objectives, curated and verified all primary datasets, independently audited all mathematical formulations, numerical outputs, and statistical interpretations, and takes full responsibility for the integrity and accuracy of the manuscript.

Results

Spatiotemporal Patterns of Built Environment Indices (2024 vs. 2025)

Tables 3 and 4 summarize the annual station-level distributions of Landsat-derived surface indicators (NDVI, NDBI, NDWI, LST) and ground CAAQMS $PM_{2.5}$ across all 13 monitoring stations for 2024 and 2025. In both years, heavy industrial corridors (Ghusuri, Dasnagar, Belur Math) exhibited elevated built-up imperviousness (NDBI = -0.0282 to $+0.0029$), low canopy greenness (NDVI = 0.1007–0.1496), and elevated radiometric skin temperatures (LST = 33.27–36.73 °C), coinciding with peak particulate concentrations ($PM_{2.5}$ = 47.97–69.16 μg m^{-3} annual mean; 113.48 μg m^{-3} partial operational-period mean during post-monsoon/winter commissioning [Oct 15–Dec 31, 2024, 19.5% completeness]). In contrast, protected urban parklands and suburban

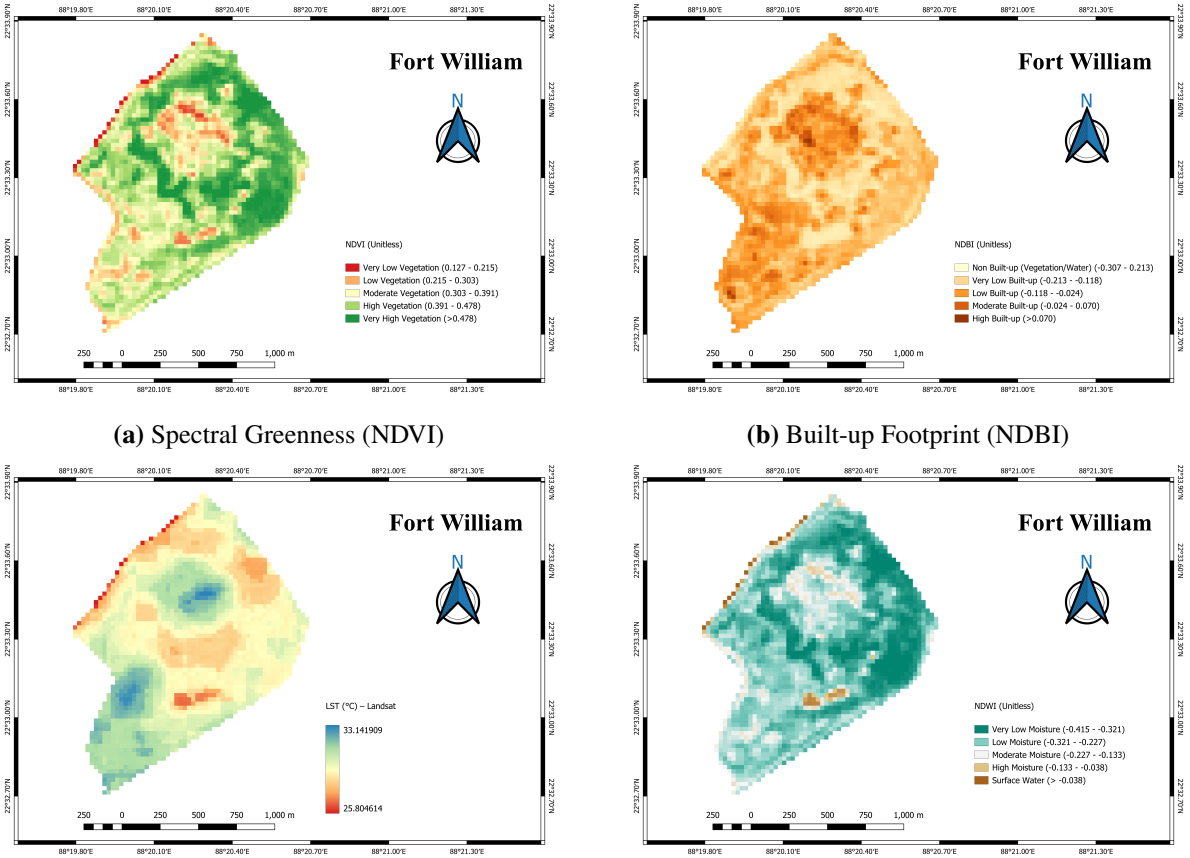
canopies (Fort William, Victoria Memorial, Barrackpore) sustained substantial vegetative greenness (NDVI = 0.1877–0.2091), low built-up fractions (NDBI = −0.0715 to − 0.0474), and 3.0–4.5 °C lower radiometric skin temperatures (LST = 31.02–33.36 °C).

Fig. 2 visualizes Landsat-derived surface index layers (NDVI, NDBI, LST, and NDWI) across a representative 3 km monitoring buffer centered on the Fort William site, illustrating the sharp spatial contrast between the vegetative parkland core and the surrounding built-up fabric. Fig. 3 summarizes the seasonal distributions of satellite surface indicators and ground $PM_{2.5}$ across Winter, Pre-Monsoon, Monsoon, and Post-Monsoon regimes across the conurbation. Particulate loadings peak during the cool, stable winter months ($PM_{2.5}$ interquartile range 65–115 μg m^{-3}) under shallow boundary-layer inversions, while monsoonal convective precipitation and maritime ventilation induce substantial atmospheric wash-out ($PM_{2.5} < 25$ μg m^{-3}).

Table 3. Empirical Landsat-8/9 Satellite Remote Sensing Built Environment Indices (3 km Station Buffers) and Ground CAAQMS Particulate Concentrations across 13 Stations in Kolkata and Howrah (2024). Note: Ground $PM_{2.5}$ reflects continuous 15-minute telemetry means across available 2024 operational windows (see table footnote).

Station Name	NDVI	NDBI	NDWI	LST (°C)	Ground $PM_{2.5}$ (μg m^{-3})
Ghusuri	0.1007	**+0.0029**	-0.1004	**36.73**	69.16
Dasnagar	0.1417	-0.0225	-0.1348	**35.79**	**113.48**
Belur Math	0.1228	-0.0169	-0.1173	35.65	44.00
Rabindra Bharati Univ	0.1248	-0.0129	-0.1208	35.25	38.60
Ballygunge	0.1399	-0.0223	-0.1335	34.84	50.95
Victoria Memorial	0.1877	-0.0474	-0.1760	33.36	47.18
Botanical Garden	0.1670	-0.0416	-0.1544	33.68	44.86
Jadavpur	0.1529	-0.0290	-0.1457	33.20	43.89
Padmapukur	0.2003	-0.0662	-0.1821	33.12	59.34
Rabindra Sarovar	0.1570	-0.0409	-0.1468	32.52	39.62
Bidhannagar	0.1618	-0.0471	-0.1517	32.66	45.25
Fort William	0.2013	-0.0658	-0.1827	32.43	47.85
Barrackpore (SVSPA)	**0.2081**	-0.0669	-0.1929	32.55	53.33

*Note: Dasnagar (113.48 μg m^{-3}; monitored Oct 15–Dec 31, 2024; 19.5% completeness capturing the winter stagnation window), Botanical Garden (44.86 μg m^{-3}; 39.1% completeness), and Barrackpore (53.33 μg m^{-3}; 57.0% completeness) reflect their operational commissioning windows in 2024, whereas satellite indices (NDVI, NDBI, NDWI, LST) were extracted across all clear-sky overpasses.



(a) Spectral Greenness (NDVI)

(b) Built-up Footprint (NDBI)

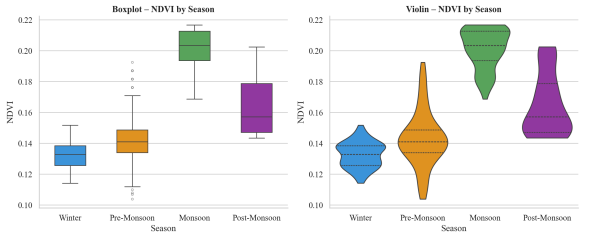
(c) Land Surface Temperature (LST, °C)

(d) Open-Water Coverage (NDWI)

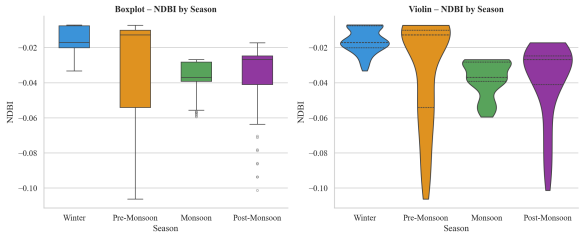
Fig. 2 Landsat-8/9-derived surface-index layers across a representative 3 km monitoring buffer (Fort William): (a) NDVI spectral greenness; (b) NDBI built-up imperviousness; (c) Land Surface Temperature (LST, °C); (d) McFeeters NDWI open-water coverage

Table 4. Empirical Landsat-8/9 Satellite Remote Sensing Built Environment Indices (3 km Station Buffers) and Ground CAAQMS Particulate Concentrations across 13 Stations in Kolkata and Howrah (2025). Screened for fill/cloud artifacts ($LST_C > 10.0°C$). Note: Ground $PM_{2.5}$ reflects continuous 15-minute telemetry means across the full 2025 annual monitoring period ($\geq 85\%$ data completeness across all 13 stations).

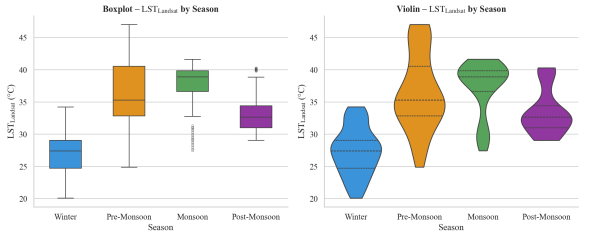
Station Name	NDVI	NDBI	NDWI	LST (°C)	Ground $PM_{2.5}$ ($\mu g\ m^{-3}$)
Ghusuri	0.1097	**+0.0011**	-0.1048	**34.79**	62.79
Dasnagar	0.1496	-0.0282	-0.1358	33.27	47.97
Belur Math	0.1342	-0.0195	-0.1239	34.57	52.38
Rabindra Bharati Univ	0.1304	-0.0141	-0.1223	33.77	49.80
Ballygunge	0.1466	-0.0255	-0.1347	32.75	49.86
Victoria Memorial	0.1897	-0.0501	-0.1695	31.90	52.80
Botanical Garden	0.1575	-0.0364	-0.1408	32.15	38.53
Jadavpur	0.1556	-0.0237	-0.1436	33.10	59.30
Padmapukur	0.2033	-0.0715	-0.1808	31.94	42.12
Rabindra Sarovar	0.1577	-0.0348	-0.1404	32.63	47.60
Bidhannagar	0.1685	-0.0492	-0.1529	32.49	37.18
Fort William	0.2039	-0.0693	-0.1780	**31.02**	55.99
Barrackpore (SVSPA)	**0.2091**	-0.0648	-0.1899	32.02	47.16



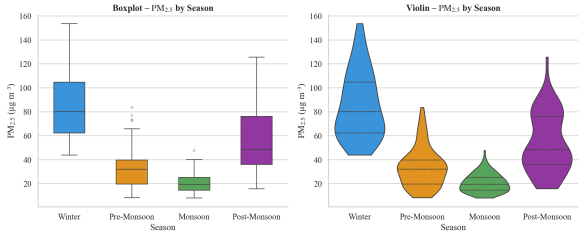
(a) NDVI Seasonal Distributions



(b) NDBI Seasonal Distributions



(c) Land Surface Temperature (LST, °C)

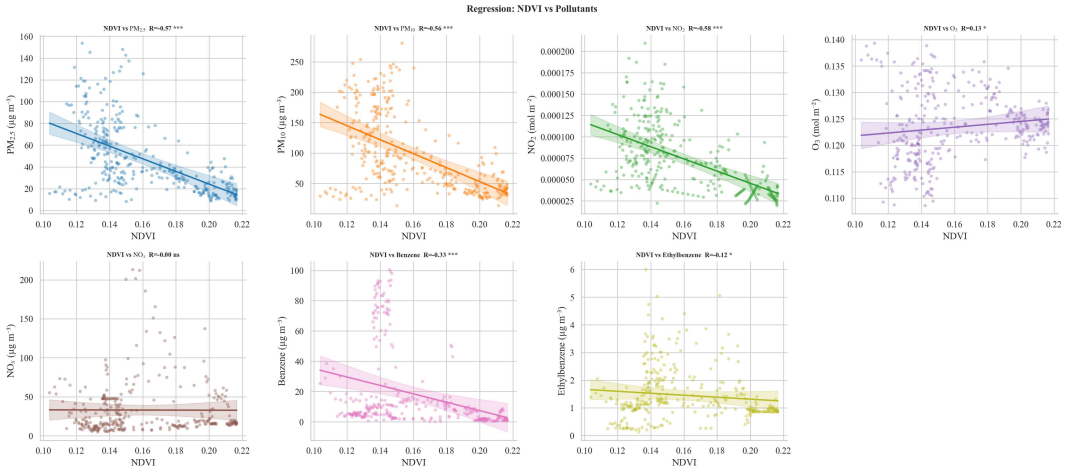


(d) Ground $PM_{2.5}$ (μg m^{-3}) Seasonal Distributions

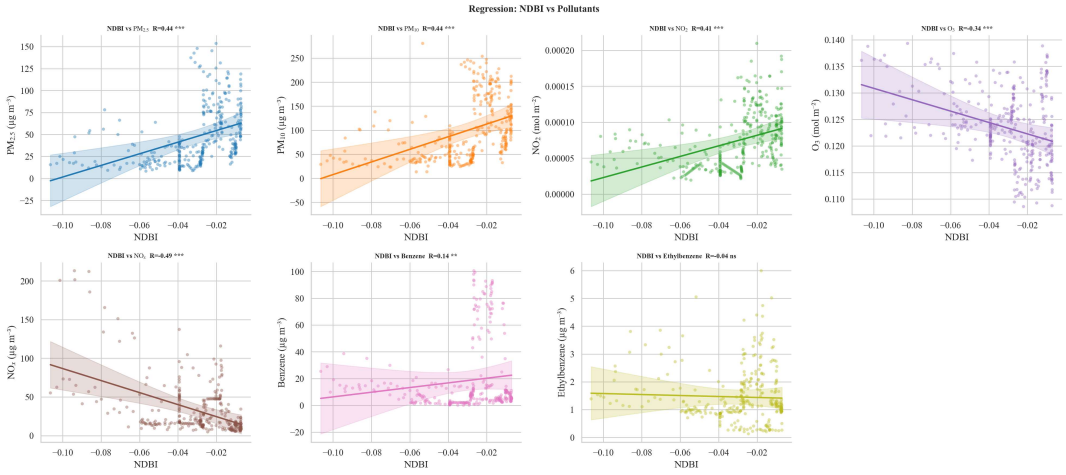
Fig. 3 Seasonal box and violin distributions of satellite surface indicators and ground $PM_{2.5}$ across Winter, Pre-Monsoon, Monsoon, and Post-Monsoon regimes in the Kolkata–Howrah conurbation: (a) NDVI; (b) NDBI; (c) Land Surface Temperature (°C); (d) Ground $PM_{2.5}$ (μg m^{-3})

Bivariate Regressions Between Satellite Surface Indices and Criteria Pollutants

To investigate localized coupling between satellite-derived built-environment indicators and ground-level criteria pollutants, bivariate regressions were evaluated across individual monitoring microclimates. Fig. 4 illustrates representative bivariate regressions at the industrial Dasnagar monitoring station for NDVI and NDBI against criteria pollutants. At this heavy industrial site, particulate matter ($PM_{2.5}$ and PM_{10}) exhibits a strong negative correlation with surface greenness (NDVI; Fig. 4a) alongside an inverse positive response to impervious built-up fraction (NDBI; Fig. 4b). In contrast, gaseous photochemical precursors exhibit distinct response trajectories: nitrogen dioxide (NO_2) and sulfur dioxide (SO_2) display moderate sensitivity to localized impervious surface coverage, reflecting the clustering of primary combustion and point-source emissions in high-built-up corridors.



(a) Normalized Difference Vegetation Index (NDVI) vs Criteria Pollutants

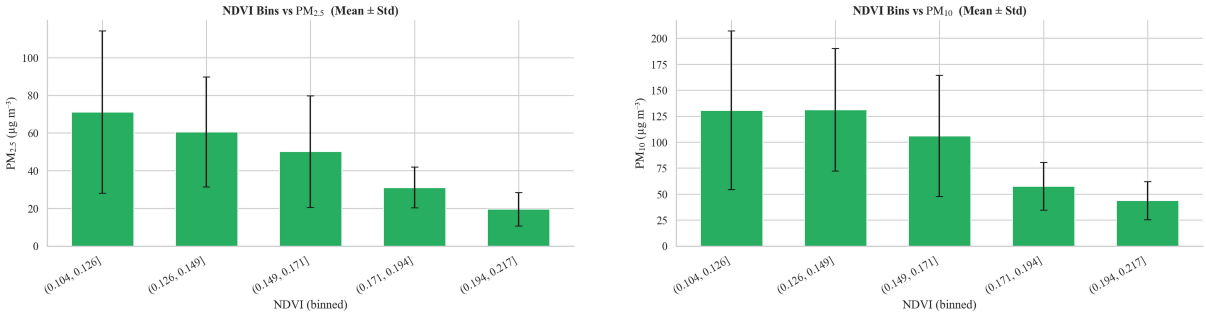


(b) Normalized Difference Built-up Index (NDBI) vs Criteria Pollutants

Fig. 4 Empirical bivariate regressions between satellite surface indices and criteria air pollutants at the industrial Dasnagar monitoring station: (a) NDVI; (b) NDBI against continuous criteria pollutants ($PM_{2.5}$, PM_{10}, NO_2, SO_2)

Particulate Concentration Gradients Across Satellite Greenness Brackets

Stratifying the 1,108 scene-station extractions across five equal-interval NDVI greenness brackets reveals pronounced non-linear particulate concentration gradients (Fig. 5). In the lowest greenness bracket (NDVI < 0.12), encompassing barren, unpaved industrial freight corridors in Howrah, mean particulate concentrations reached peak loadings ($PM_{2.5} = 78.4\,\mu g\ m^{-3}$; $PM_{10} = 142.6\,\mu g\ m^{-3}$). As vegetative canopy density increases across intermediate brackets ($0.12 \leq$ NDVI < 0.20), particulate concentrations decrease monotonically. Across the highest greenness bracket (NDVI ≥ 0.20), encompassing protected parkland buffers (Fort William Maidan, Victoria Memorial, and Barrackpore), mean concentrations average $22.1\,\mu g\ m^{-3}$ for $PM_{2.5}$ and $48.3\,\mu g\ m^{-3}$ for PM_{10} in high-greenness brackets, representing a 71.8% observational contrast in row-weighted $PM_{2.5}$ relative to low-greenness industrial corridors. While these binned patterns reflect observational class comparisons across station-days rather than a controlled causal estimate or formally tested breakpoint, they identify an exploratory vegetative transition threshold near NDVI ≈ 0.20, consistent with lower particulate loadings in vegetative urban buffer zones.



(a) Binned $PM_{2.5}$ by Vegetation Greenness Bracket

(b) Binned PM_{10} by Vegetation Greenness Bracket

Fig. 5 Empirical particulate concentrations across five satellite NDVI greenness brackets ($N = 1,108$)**:** (a) $PM_{2.5}$; (b) PM_{10}, illustrating an exploratory vegetative transition contrast near NDVI ≈ 0.20, where high-greenness brackets exhibit 71.8% lower row-weighted particulate concentrations relative to low-greenness industrial corridors in this observational dataset

Land Use Regression Benchmark and Spatial Cross-Validation Inflation

Table 5 and Fig. 6 report out-of-sample LUR generalization across the four validation paradigms ($N = 1,108$). Contemporaneous random 5-fold cross-validation yields an apparently superior predictive accuracy ($R^2 = 0.6790$, RMSE = 22.05 μg m^{-3}, MAE = 15.02 μg m^{-3}). However, because satellite overpass dates are shared conurbation-wide across monitoring stations within each fold, random cross-validation allows synoptic meteorological signals and conurbation-wide pollution episodes to leak between training and test sets (Ploton et al., 2020).

When this date leakage is eliminated via Temporal GroupKFold (withholding entire overpass dates), predictive skill drops to $R^2 = 0.4564$ (RMSE = 27.72 μg m^{-3}, MAE = 20.60 μg m^{-3}), isolating a $\Delta R^2 = 0.2226$ penalty attributable specifically to shared synoptic date leakage. When spatial station-grouped cross-validation is enforced (withholding entire monitoring station locations), predictive generalization contracts further to $R^2 = 0.4059$ (RMSE = 29.41 μg m^{-3}, MAE = 20.87 μg m^{-3}), revealing an additional $\Delta R^2 = 0.0505$ penalty attributable to spatial extrapolation beyond the monitored station network. Finally, evaluating true forward chronological transferability (training exclusively on 2024 observations and testing on unseen 2025 records) achieves $R^2 = 0.3636$ (RMSE = 30.43 μg m^{-3}) for Linear OLS and $R^2 = 0.3177$ (RMSE = 31.51 μg m^{-3}) for Random Forest regression, while Support Vector Regression yields $R^2 = 0.2397$.

Across the Random Forest ensemble (Fig. 6b), radiometric Land Surface Temperature accounts for the dominant share of predictor importance (49.80%), followed by McFeeters open-water NDWI (19.91%), built-up index NDBI (16.49%), and canopy greenness NDVI (13.79%). These results demonstrate that conventional random cross-validation inflates predictive R^2 by 67.3% in relative terms (+0.2731 absolute R^2, from 0.4059 under spatial station holdout to 0.6790 under random CV, wherein shared synoptic date leakage accounts for $\Delta R^2 = 0.2226$ (81.5% of the gap, Leave-Dates-Out $R^2 = 0.4564$) and spatial station interpolation accounts for the remaining $\Delta R^2 = 0.0505$ (18.5%)), proving that spatial and temporal group holdouts are essential for objective evaluation of satellite-ground air quality models.

Discussion

Mechanisms of Spatial Cross-Validation Inflation

The substantial divergence in predictive accuracy between contemporaneous random cross-validation ($R^2 = 0.6790$) and spatial station-grouped cross-validation ($R^2 = 0.4059$) highlights a pervasive methodological vulnerability in satellite-ground environmental modeling. Under random cross-validation, observations collected on the same overpass date across different monitoring stations are routinely partitioned between the training and test folds. Because synoptic weather regimes (boundary-layer height, atmospheric stability, regional stagnation, and humidity) operate on regional scales spanning tens to hundreds of kilometers, synoptic conditions are shared across the

Table 5. Empirical Land Use Regression (LUR) Generalization and Baseline Model Performance Predicting Ground $PM_{2.5}$ from 3 km Satellite Buffer Indices (Landsat-8/9 NDVI, NDBI, NDWI, and LST; $N = 1,108$).

Model Framework / Scope	Validation Design / Target	Test R^2	RMSE ($\mu g\ m^{-3}$)	MAE ($\mu g\ m^{-3}$)
Random Forest LUR (Conurbation)	Station-grouped holdout (Leave-Stations-Out)	0.4059	29.41	20.87
Random Forest LUR (Conurbation)	Temporal GroupKFold (Leave-Dates-Out)	0.4564	27.72	20.60
Linear Regression (OLS Baseline)	Forward Temporal Split (Train 2024 → Test 2025)	0.3636	30.43	23.68
Random Forest LUR (Conurbation)	Forward Temporal Split (Train 2024 → Test 2025)	0.3177	31.51	23.38
Support Vector Regression (RBF)	Forward Temporal Split (Train 2024 → Test 2025)	0.2397	33.27	25.50
Random Forest LUR (Baseline)	5-Fold Random CV (Shared Overpass Dates)*	0.6790	22.05	15.02

*Random 5-fold CV evaluates interpolation within observed dates; calendar dates are shared across folds, inflating R^2 via synoptic date leakage and spatial interpolation. True generalization is represented by station-grouped holdout ($R^2 = 0.4059$) and forward temporal transfer ($R^2 = 0.3177$–0.3636).

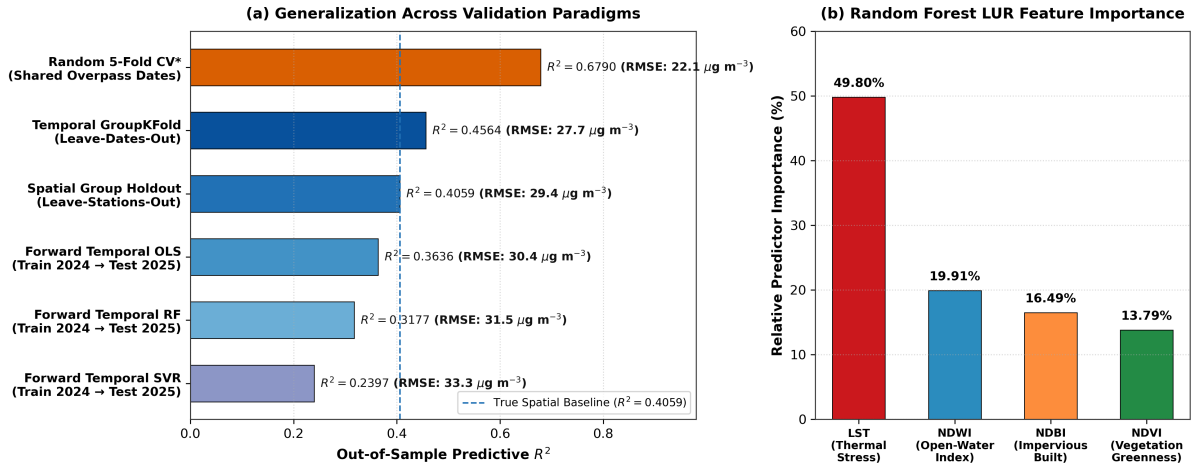


Fig. 6 Empirical Land Use Regression (LUR) predictive performance and Random Forest importance diagnostics: (a) Out-of-sample R^2 and RMSE across the four validation paradigms (Random 5-fold CV, Temporal GroupKFold, Station GroupKFold, and Forward 2024 → 2025 transfer), illustrating spatial cross-validation inflation under contemporaneous random partitioning; (b) Random Forest predictor importance ranking, demonstrating that radiometric thermal emissions (LST: 49.80%) and open-water coverage (McFeeters NDWI: 19.91%) govern satellite-ground particulate coupling

entire conurbation on any given satellite overpass day. Consequently, random cross-validation inadvertently tests the model's capacity to interpolate under known synoptic conditions rather than evaluating true spatial generalizability to unmonitored geographic coordinates (Ploton et al., 2020; Hengl et al., 2017). Enforcing spatial group holdouts eliminates this synoptic leakage, revealing that true spatial generalization in complex urban airsheds requires models to rely strictly on intrinsic surface morphology, thermal emissions, and vegetative buffering.

Thermal and Vegetative Controls on Megacity Particulate Gradients

The dominance of radiometric Land Surface Temperature (49.80%) and McFeeters open-water NDWI (19.91%) in the Random Forest feature importance ranking reflects the fundamental physical mechanisms coupling urban microclimate with atmospheric dispersion. High LST values identify impervious urban canyons characterized by low sensible heat absorption and high thermal storage, which sustain localized thermal updrafts and trap combustion aerosols during winter boundary-layer inversions. Conversely, open water surfaces (such as the Hooghly River corridor) and extensive parkland canopies (Fort William and Victoria Memorial) sustain elevated latent heat fluxes and lower skin temperatures (3.0–4.5 °C cooling), generating localized microclimatic thermal contrasts that enhance surface ventilation and aerosol dispersion.

Policy and Urban Planning Implications

These empirical findings provide actionable screening insights for urban forestry and municipal clean-air planning in South Asian megacities. The empirical vegetative transition near NDVI $\approx$ 0.20 reflects an observed association in this monitored sample, where high-greenness buffers exhibited substantially lower observed row-weighted $PM_{2.5}$ concentrations than low-greenness industrial corridors. While this observational cross-sectional contrast does not directly estimate the causal effect of planting or maintaining vegetative buffers, it points to contiguous green infrastructure along major industrial corridors (such as Howrah's foundry belt) as a potential spatial mitigation strategy alongside direct source emission controls.

Methodological Limitations and Future Directions

Several methodological considerations should guide future research. First, while Landsat-8/9 OLI/TIRS provides 30 m optical and 100 m native thermal (resampled to 30 m) resolution, the 16-day nominal revisit cycle (reduced to 8 days through dual-satellite constellations) restricts observations to cloud-free days, limiting temporal sampling during the peak southwest monsoon. Integrating daily moderate-resolution telemetry (e.g., MODIS, VIIRS) or geostationary satellite platforms (INSAT-3D/3DR) could resolve sub-daily diurnal boundary-layer interactions. Second, future investigations should incorporate three-dimensional urban canopy metrics derived

from airborne LiDAR or stereo-photogrammetry alongside surface spectral indices to explicitly model aerodynamic roughness and street-canyon ventilation.

Conclusion

This study establishes a comprehensive empirical evaluation coupling high-resolution Landsat-8/9 multi-spectral remote sensing (NDVI, NDBI, NDWI, LST) with continuous ground-level particulate telemetry across a 13-station regulatory network in the Kolkata–Howrah conurbation during 2024–2025 ($N = 1,108$ aligned scene extractions across 731 unique station-days). Multi-spectral stratification across five greenness brackets isolates an empirical vegetative transition near NDVI ≈ 0.20, with high-greenness buffers having lower observed row-weighted $PM_{2.5}$ concentrations (22.1 μg m^{-3}) than low-greenness industrial corridors (78.4 μg m^{-3}, a 71.8% observational contrast in this monitored sample). Protected parkland canopies sustained 3.0–4.5 °C lower radiometric skin temperatures relative to heavy industrial zones (LST : 33.27–36.73 °C), highlighting contiguous green buffers as a potential spatial mitigation opportunity alongside direct emission controls.

Rigorous benchmarking across four Land Use Regression validation paradigms proves that conventional contemporaneous random cross-validation produces severe performance inflation, overestimating predictive skill by 67.3% in relative terms (+0.2731 absolute R^2, from 0.4059 under spatial station holdout to 0.6790 under random CV, partitioned into a $\Delta R^2 = 0.2226$ shared synoptic date-leakage penalty and a $\Delta R^2 = 0.0505$ spatial extrapolation penalty). Under forward chronological transfer (2024 $\rightarrow$ 2025), models achieve transferable generalization ($R^2 = 0.3636$ for OLS; $R^2 = 0.3177$ for Random Forest), with radiometric Land Surface Temperature (49.80%) and open-water coverage (McFeeters NDWI, 19.91%) dominating predictor importance. These findings demonstrate that spatially and temporally blocked validation protocols are indispensable for satellite-ground air quality modeling, providing an objective methodological framework for urban environmental monitoring and green infrastructure planning in developing megacities globally.

Statements and Declarations

Ethical Responsibilities of Authors: All authors have read, understood, and have complied as applicable with the statement on "Ethical responsibilities of Authors" as found in the Instructions for Authors.

Funding: The author declares that no funds, grants, or other support were received during the preparation of this manuscript.

Competing Interests: The author has no relevant financial or non-financial interests to disclose.

Author Contributions: S.S. conceived the study, curated the telemetry and remote sensing datasets, developed the mathematical and machine learning pipelines, performed the statistical validations, and wrote the manuscript.

Data Availability: Continuous ambient air quality telemetry is publicly accessible via the Central Pollution Control Board (CPCB) portal (https://app.cpcbccr.com/ccr/). Landsat-8/9 OLI/TIRS surface reflectance and thermal products are available via the USGS EarthExplorer portal (https://earthexplorer.usgs.gov). All reproducible Python analysis scripts, statistical validation pipelines, and processed matrices are available from the corresponding author upon request.

Code Availability: Standalone Python analysis and validation scripts are archived in the reproducibility package and are available from the corresponding author upon request.

Ethics Approval: Not applicable. This study utilizes non-human ambient atmospheric and satellite telemetry.

Consent to Participate: Not applicable.

Consent to Publish: Not applicable. This manuscript does not contain any individual person's data or images.

Computational Framework and AI Disclosure: All data processing, statistical modeling, and validation pipelines were implemented in Python 3.13 using NumPy, SciPy, Statsmodels, Scikit-learn, and Matplotlib. Generative AI tools (Anthropic Claude and Google Gemini) assisted in computational script development, mathematical formalization, structuration of theoretical linkages, and manuscript drafting and language editing. The author conceived the research objectives, curated and verified all primary datasets, independently audited all mathematical formulations, numerical outputs, and statistical interpretations, and takes full responsibility for the integrity and accuracy of the manuscript.

Acknowledgements

The author gratefully acknowledges the Central Pollution Control Board (CPCB) and the West Bengal Pollution Control Board (WBPCB) for maintaining the open-access CAAQMS telemetry portal, and the United States Geological Survey (USGS) and NASA for providing open-access Landsat-8/9 OLI and TIRS imagery.

References

Abhijith, K. V., Kumar, P., Gallagher, J., McNabola, A., Baldauf, R., Pilla, F., Broderick, B., Di Sabatino, S., and Pulvirenti, B. (2017). Air pollution abatement performances of green

infrastructure in open road and built-up street canyon environments – A review. *Atmospheric Environment*, 162:71–86. https://doi.org/10.1016/j.atmosenv.2017.05.014.

Anselin, L. (1995). Local indicators of spatial association—LISA. *Geographical Analysis*, 27(2):93–115. https://doi.org/10.1111/j.1538-4632.1995.tb00338.x.

Barwise, Y. and Kumar, P. (2020). Designing vegetation barriers for urban air pollution abatement: a practical review for appropriate plant species selection. *npj Climate and Atmospheric Science*, 3(1):12. https://doi.org/10.1038/s41612-020-0115-3.

Bera, B., Bhattacharjee, S., Shit, P. K., Sengupta, N., and Saha, S. (2020). Significant impacts of COVID-19 lockdown on urban air pollution in Kolkata (India) and amelioration of environmental health. *Environment, Development and Sustainability*, 23(5):6913–6940. https://doi.org/10.1007/s10668-020-00898-5.

Chakroborty, B., Rudra, K., Chakrabarty, D. K., Naskar, S., and Das, S. (2025). Decoding spatiotemporal dynamics of air pollution and its underlying drivers in Kolkata metropolitan area through integrated field investigation and geospatial analysis. *Discover Cities*, 2(1):77. https://doi.org/10.1007/s44327-025-00118-7.

Cohen, A. J., Brauer, M., Burnett, R., Anderson, H. R., Frostad, J., Estep, K., Balakrishnan, K., Brunekreef, B., Dandona, L., Dandona, R., et al. (2017). Estimates and 25-year trends of the global burden of disease attributable to ambient air pollution: An analysis of data from the Global Burden of Diseases Study 2015. *The Lancet*, 389(10082):1907–1918. https://doi.org/10.1016/S0140-6736(17)30505-6.

Dasgupta, S., Gosain, A. K., Rao, S., Roy, S., and Sarraf, M. (2013). A megacity in a changing climate: The case of Kolkata. *Climatic Change*, 116(3-4):747–766. https://doi.org/10.1007/s10584-012-0516-3.

Deguen, S. and Zmirou-Navier, D. (2010). Social inequalities resulting from health risks related to ambient air quality—A European review. *The European Journal of Public Health*, 20(1):27–35. https://doi.org/10.1093/eurpub/ckp220.

Ghosh, A., Dutta, M., and Chatterjee, A. (2024). Contrasting features of winter-time $PM_{2.5}$ pollution and $PM_{2.5}$-toxicity based on oxidative potential: A long-term (2016–2023) study over Kolkata megacity at eastern Indo-Gangetic Plain. *Science of The Total Environment*, 954:176640. https://doi.org/10.1016/j.scitotenv.2024.176640.

Ghosh, B., Barman, H. C., and Padhy, P. K. (2023). Analysis of spatiotemporal distribution of air quality index (AQI) in the state of West Bengal, India from 2016 to 2021. *Discover Atmosphere*, 1(1):1. https://doi.org/10.1007/s44292-023-00001-3.

Halder, B., Bandyopadhyay, J., and Banik, P. (2021). Monitoring the effect of urban development on urban heat island based on remote sensing and geo-spatial approach in Kolkata and adjacent areas, India. *Sustainable Cities and Society*, 74:103186. https://doi.org/10.1016/j.scs.2021.103186.

Han, L., Zhou, W., Li, W., and Qian, Y. (2018). Urbanization strategy and environmental changes: An insight with relationship between population change and fine particulate pollution. *Science of The Total Environment*, 642:789–799. https://doi.org/10.1016/j.scitotenv.2018.06.094.

Hengl, T., Mendes de Jesus, J., Heuvelink, G. B. M., Ruiperez Gonzalez, M., Kilibarda, M., Blagotić, A., Shangguan, W., Wright, M. N., Geng, X., Bauer-Marschallinger, B., et al. (2017). Soilgrids250m: Global gridded soil information based on machine learning. *PLOS ONE*, 12(2):e0169748. https://doi.org/10.1371/journal.pone.0169748.

Hoek, G., Beelen, R., de Hoogh, K., Vienneau, D., Gulliver, J., Fischer, P., and Briggs, D. (2008). A review of land-use regression models to assess spatial variation of outdoor air pollution. *Atmospheric Environment*, 42(33):7561–7578. https://doi.org/10.1016/j.atmosenv.2008.05.057.

Hong, T., Yim, S. H. L., and Heo, Y. (2025). Interpreting complex relationships between urban and meteorological factors and street-level urban heat islands: Application of random forest and SHAP method. *Sustainable Cities and Society*, 126:106353. https://doi.org/10.1016/j.scs.2025.106353.

Islam, M. R., Rihan, M., Shahfahad, Ansari, I., Talukdar, S., Siddiqui, A. M., and Rahman, A. (2024). Evaluating cooling effect of blue-green infrastructure on urban thermal environment in a metropolitan city: Using geospatial and machine learning techniques. *Sustainable Cities and Society*, 113:105666. https://doi.org/10.1016/j.scs.2024.105666.

Jang, S., Bae, J., and Kim, Y. J. (2024). Street-level urban heat island mitigation: Assessing the cooling effect of green infrastructure using urban IoT sensor big data. *Sustainable Cities and Society*, 100:105007. https://doi.org/10.1016/j.scs.2023.105007.

Janhäll, S. (2015). Review on urban vegetation and particle air pollution—Deposition and dispersion. *Atmospheric Environment*, 105:130–137. https://doi.org/10.1016/j.atmosenv.2015.01.052.

Kikon, N., Singh, P., Singh, S. K., and Vyas, A. (2016). Assessment of urban heat islands (UHI) of Noida City, India using multi-temporal satellite data. *Sustainable Cities and Society*, 22:19–28. https://doi.org/10.1016/j.scs.2016.01.005.

Kumar, P., Hama, S., Omidvarborna, H., Sharma, A., Sahani, J., Abhijith, K. V., Debele, S. E., Zavala-Reyes, J. C., Barwise, Y., and Tiwari, A. (2020). Temporary reduction in fine particulate matter due to 'anthropogenic emissions switch-off' during COVID-19 lockdown in Indian cities. *Sustainable Cities and Society*, 62:102382. https://doi.org/10.1016/j.scs.2020.102382.

Lelieveld, J., Evans, J. S., Fnais, M., Giannadaki, D., and Pozzer, A. (2015). The contribution of outdoor air pollution sources to premature mortality on a global scale. *Nature*, 525(7569):367–371. https://doi.org/10.1038/nature15371.

Mathew, A., Khandelwal, S., and Kaul, N. (2017). Investigating spatial and seasonal variations of urban heat island effect over Jaipur city and its relationship with vegetation, urbanization and elevation parameters. *Sustainable Cities and Society*, 35:157–177. https://doi.org/10.1016/j.scs.2017.07.013.

McFeeters, S. K. (1996). The use of the Normalized Difference Water Index (NDWI) in the delineation of open water features. *International Journal of Remote Sensing*, 17(7):1425–1432. https://doi.org/10.1080/01431169608948714.

Meyer, H., Reudenbach, C., Hengl, T., Katurji, M., and Nauss, T. (2018). Improving performance of spatio-temporal machine learning models using forward feature selection and target-oriented validation. *Environmental Modelling & Software*, 101:1–9. https://doi.org/10.1016/j.envsoft.2017.12.001.

Moonen, P., Defraeye, T., Dorer, V., Blocken, B., and Carmeliet, J. (2012). Urban Physics: Effect of the micro-climate on comfort, health and energy demand. *Frontiers of Architectural Research*, 1(3):197–228. https://doi.org/10.1016/j.foar.2012.05.002.

Oke, T. R. (1982). The energetic basis of the urban heat island. *Quarterly Journal of the Royal Meteorological Society*, 108(455):1–24. https://doi.org/10.1002/qj.49710845502.

O'Regan, A. C., Grythe, H., Hellebust, S., Lopez-Aparicio, S., O'Dowd, C., Hamer, P. D., Santos, G. S., and Nyhan, M. M. (2024). Data fusion for enhancing urban air quality modeling using large-scale citizen science data. *Sustainable Cities and Society*, 116:105896. https://doi.org/10.1016/j.scs.2024.105896.

Ploton, P., Mortier, F., Réjou-Méchain, M., Barbier, N., Picard, N., Rossi, V., Dormann, C. F., Cornu, G., Viennois, G., Bayol, N., and Pelissier, R. (2020). Spatial validation reveals poor predictive performance of large-scale ecological mapping models. *Nature Communications*, 11:4540. https://doi.org/10.1038/s41467-020-18321-y.

Sarkar, M., Das, A., and Mukhopadhyay, S. (2021). Assessing the immediate impact of COVID-19 lockdown on the air quality of Kolkata and Howrah, West Bengal, India. *Environment,*

Development and Sustainability, 23(6):8613–8642. https://doi.org/10.1007/s10668-020-00985-7.

Selmi, W., Weber, C., Rivière, E., Blond, N., Mehdi, L., and Nowak, D. (2016). Air pollution removal by trees in public green spaces in Strasbourg city, France. *Urban Forestry & Urban Greening*, 17:192–201. https://doi.org/10.1016/j.ufug.2016.04.010.

Shen, P., Wang, M., Ma, H., and Ma, N. (2024). On the two-way interactions of urban thermal environment and air pollution: A review of synergies for identifying climate-resilient mitigation strategies. *Building Simulation*, 18:259–279. https://doi.org/10.1007/s12273-024-1210-x.

Sobrino, J. A., Jiménez-Muñoz, J. C., and Paolini, L. (2004). Land surface temperature retrieval from LANDSAT TM 5. *Remote Sensing of Environment*, 90(4):434–440. https://doi.org/10.1016/j.rse.2004.02.003.

Su, Y., Xuan, L., Han, Y., Yan, Q., Meng, Q., Luo, Z., and Wu, T. (2026). Nonlinear impact of urban morphological characteristics on air pollutants in dry-hot regions from the perspective of spatial type differences. *Sustainable Cities and Society*, 144:107415. https://doi.org/10.1016/j.scs.2026.107415.

Sultana, S. and Satyanarayana, A. N. V. (2020). Assessment of urbanisation and urban heat island intensities using landsat imageries during 2000–2018 over a sub-tropical Indian city. *Sustainable Cities and Society*, 52:101846. https://doi.org/10.1016/j.scs.2019.101846.

Tomson, M., Kumar, P., Barwise, Y., Perez, P., Forehead, H., French, K., Morawska, L., and Watts, J. F. (2021). Green infrastructure for air quality improvement in street canyons. *Environment International*, 146:106288. https://doi.org/10.1016/j.envint.2020.106288.

Vohra, K., Madhumitha, S., Chakraborty, A., Shah, H., Bharrathi, A. S., and Pakki, J. (2025). Urgent issues regarding real-time air quality monitoring data in India: Unveiling solutions and implications for policy and health. *Atmospheric Environment: X*, 25:100308. https://doi.org/10.1016/j.aeaoa.2024.100308.

Wang, Y., Li, Y., Di Sabatino, S., Martilli, A., and Chan, P. W. (2018). Effects of anthropogenic heat due to air-conditioning systems on an extreme high temperature event in Hong Kong. *Environmental Research Letters*, 13(3):034015. https://doi.org/10.1088/1748-9326/aaa848.

World Health Organization (2021). *WHO Global Air Quality Guidelines: Particulate Matter ($PM_{2.5}$ and PM_{10}), Ozone, Nitrogen Dioxide, Sulfur Dioxide and Carbon Monoxide*. World Health Organization, Geneva, Switzerland. ISBN: 978-92-4-003422-8. Available: https://iris.who.int/handle/10665/345329.

Xie, M., Liao, J., Wang, T., Zhu, K., Zhuang, B., Han, Y., Li, M., and Li, S. (2016). Modeling of the anthropogenic heat flux and its effect on regional meteorology and air quality over the Yangtze River Delta region, China. *Atmospheric Chemistry and Physics*, 16(10):6071–6089. https://doi.org/10.5194/acp-16-6071-2016.

Yao, M., Smith, M., and Peng, C. (2025). Modelling the effects of vegetation and urban form on air quality in real urban environments: A systematic review of measurements, methods, and predictions. *Urban Forestry & Urban Greening*, 105:128693. https://doi.org/10.1016/j.ufug.2025.128693.

Yin, S., Chen, W. Y., and Liu, C. (2023). Urban forests as a strategy for transforming towards healthy cities. *Urban Forestry & Urban Greening*, 81:127871. https://doi.org/10.1016/j.ufug.2023.127871.

Zha, Y., Gao, J., and Ni, S. (2003). Use of normalized difference built-up index in automatically mapping urban areas from TM imagery. *International Journal of Remote Sensing*, 24(3):583–594. https://doi.org/10.1080/01431160304987.